Magneto-optical studies of hybrid organic/inorganic perovskite: The case of methyl-ammonium lead bromide

Uyen N. Huynh [1,*] Rikard Bodin,[1,*] Xin Pan,[1] Paul Bailey,[1] Haoliang Liu [1,†] Stephen McGill [2]
Dmitry Semenov [2] Peter C. Sercel [3] and Z. Valy Vardeny [1,‡]

[1]*Physics & Astronomy Department, University of Utah, Salt Lake City, Utah 84112, USA*
[2]*National High Magnetic Field Laboratory Tallahassee, Florida 32310, USA*
[3]*Center for Hybrid Organic–Inorganic Semiconductors for Energy Golden, Colorado 80401, USA*

Picosecond time-resolved and cw magneto-optical methods have been used for studying the spin-related properties of excitons and photocarriers in methyl-ammonium lead bromide (MAPbBr$_3$) thin film, single crystal, and light-emitting diodes (LED), focusing on the Landé g values of these species. Using the transient circularly polarized photoinduced quantum beatings (QB) under an applied magnetic field, **B** in MAPbBr$_3$ *single crystal,* we obtained the anisotropic g values of electrons for **B** field along [010] and [001]: $|g^e_{[001]}| = 2.15$ and $|g^e_{[010]}| = 1.75$, and for holes $|g^h_{[001]}| = 0.42$ and $|g^h_{[010]}| = 0.60$. We also used the magnetic circular dichroism method for measuring the bright excitons' g value, $g_{ex} = g_e + g_h = 2.5$. From these two types of measurements we conclude that $g_h > 0$ in MAPbBr$_3$. This conclusion was corroborated by measuring the magnetoelectroluminescence response of LED based on MAPbBr$_3$ active layer. The g values in single crystal and their average in films are in excellent agreement with a **k·p** model that shows similarity and difference to those of MAPbI$_3$. We also observed the influence of the Overhauser field on the QB frequencies that is induced by the dynamic nuclear polarization generated by the spin-aligned electrons using circularly polarized pump or probe beams.

I. INTRODUCTION

The hybrid organic-inorganic perovskites (HOIP) have recently generated substantial interest due to their superb optoelectronic properties that make them excellent candidates for the active layer in devices such as solar cells, light-emitting diodes (LEDs), and spintronic structures [1–4]. These perovskites have the formula ABX_3, where A and B are cations and X is a halide. In particular, the A cation is replaced with an organic component such as MA$^+$ (CH$_3$NH$_3$) or FA$^+$ (CH(NH$_2$)$_2$) and B is usually Pb. The possible chemical variations and tunability of the HOIP make them ideal for devices as this variation leads to the tunability of important parameters such as band gap and carrier mobility [5–8]. Methyl-ammonium lead bromide (MAPbBr$_3$) is an example of a popular HOIP that also benefits from the low-cost fabrication techniques since it can be solution processed and spin coated or deposited for easy device fabrication. Its low trap density [9], observed circularly polarized photoluminescence [10], and high absorption have made MAPbBr$_3$ an interesting candidate for device fabrication. In addition, long spin lifetimes have been also observed in MAPbBr$_3$ thin films [11]. The large Faraday rotation value of MAPbBr$_3$ makes

this material interesting as a Faraday rotator [12] in quantum information systems. Studying MAPbBr$_3$ helps to understand the impacts of the MA$^+$ cation on the fundamental optoelectronic properties of the bromide-based HOIP. Specifically, for understanding the mechanisms and properties of spin-related processes in these materials, such as spin-relaxation rates, the Landé g factors, and g-factor anisotropies are needed to advance spin-related applications [11–13]. Even though the electron- and hole g values and their anisotropies in MAPbBr$_3$ single crystals obtained using the magnetophotoluminescence (magneto-PL) technique were reported [14], the extracted values were determined indirectly via a model-dependent analysis of magneto-PL emission. By contrast, as shown below in our absorption-based measurements, the quantum beating reveals the magnitude of the carrier g factors of absorbing states *directly*, and the magnetic circular dichroism (MCD) measurement *directly* gives the sign and magnitude of the sum of the electron- and hole g factors.

In this work we have utilized a variety of transient and steady-state magneto-optical techniques to study the spin-related properties of MAPbBr$_3$ single crystals, thin films, and as active layer in LED. Using the time-resolved Kerr rotation (t-KR) obtained from picosecond transient circularly polarized photoinduced reflectivity [c-PPR(t)] in MAPbBr$_3$ crystal upon the application of a magnetic field in the Voigt configuration, we measured the electron- and hole spin-relaxation dynamics from the observed transient quantum beating (QB) at different magnetic fields **B**. The oscillation frequency of the QBs versus the magnetic field allowed us to extract the Landé g factor of the electrons and holes, respectively. These measurements were repeated for different crystal facets, [110] and

---

*These authors contributed equally to this work.

†Permanent address: Guangdong Provincial Key Laboratory of Semiconductor, Optoelectronic Materials and Intelligent Photonic Systems, School of Science, Harbin Institute of Technology (Shenzhen), Shenzhen 518055, China.

‡val@physics.utah.edu

[001], revealing the *g*-factor anisotropy in MAPbBr$_3$ crystal. We obtained for electrons $|g^e_{[001]}| = 2.15$ and $|g^e_{[010]}| = 1.75$, and for holes $|g^h_{[001]}| = 0.42$ and $|g^h_{[010]}| = 0.60$. These *g* values average in MAPbBr$_3$ films to $|g_e| = 1.89$ and $|g_h| = 0.54$, respectively. In order to find the hole *g*-value polarity we measured the *g* value, g_{ex}, of the bright exciton in thin MAPbBr$_3$ film using the method of magnetic circular dichroism (MCD). We found $g_{ex} = 2.5$, and since $g_{ex} = g_e + g_h$ we therefore could determine that $g_h > 0$ in MAPbBr$_3$. This conclusion is corroborated from magnetoelectroluminescence response [MEL(*B*)] of a LED based on MAPbBr$_3$ active layer. These results are in excellent agreement with a **k·p** model calculation applied to MAPbBr$_3$.

In addition, we also modified the standard t-KR measurement by fixing the circular polarization of the pump pulses, as opposed to modulating its circular polarization. The fixed circular polarization allowed us to measure the *Overhauser field*, B_N, generated by the dynamic nuclei spin polarization induced by the spin-polarized photocarriers. The Overhauser field can be seen as a change in the observed QB frequency between the modulated and fixed polarization with the same applied magnetic field. Specifically, we observed the Overhauser effect at $B = 0$, as a "zero-field oscillation" that appears with a fixed helicity pump, which explains similar results measured before in several hybrid perovskites [15–17].

II. RESULTS AND DISCUSSION

A. Experiments

The thin MAPbBr$_3$ films were prepared using a standard procedure with a precursor solution, with CH$_3$NH$_3$Br and PbBr$_2$ in a molar ratio of 1:1 in N,N-dimethylformamide forming a concentration of 0.8 mol/ml (see the Appendix). The MAPbBr$_3$ crystals were grown via antisolvent precipitation (see the Appendix). X-ray-diffraction (XRD) measurements confirm the crystal structure and principal axes [see Fig. 1(a)]. Our pump-probe measurements were conducted on a MAPbBr$_3$ crystal at 4 K for two crystal facets, namely (001) and (110) [Fig. 1(a)], with applied magnetic fields parallel to the crystal surface along [010] and [001], respectively [Fig. 1(b)].

The c-PPR(t) experiment, which was described previously [16], and the transient Kerr rotation t-KR(t) [see Fig. 1(c)] were utilized for measuring the carriers and nuclei spin dynamics in MAPbBr$_3$ crystal as detailed in the Appendix. These methods are a derivative of the more popular optical pump/probe technique, in which the pump beam was modulated by a photoelastic modulator (PEM) between left (δ^+, or LCP) and right (δ^-, or RCP) circular polarization, whereas the probe beam's circular polarization was set at LCP/RCP for the t-PPR(t) and at linear polarization (LP) for t-KR(t). We used a pump beam at 405 nm and probe beam at 552 nm which were generated using a variety of nonlinear optical crystals (such as barium borate). Our pump/probe setup had a time resolution of 250 fs at 80-MHz repetition rate. For the t-PPR(t) technique, the transient change in the probe-beam reflection induced by LCP and RCP pump polarizations, $\Delta R^{\delta^+\delta^+}_{\delta^-\delta^+} = R_{\delta^+\delta^+} - R_{\delta^-\delta^+}$, was recorded. In this scheme the c-PPR(t) dynamics is proportional to the excited state's population

difference between LCP and RCP pump excitation, which is proportional to the population difference, $N_{LCP} - N_{RCP}$. Since the LCP and RCP lights excite electrons (holes) with opposite spin alignments, therefore the c-PPR(t) reflects the spin-relaxation dynamics of the electrons' (holes') spins. For the t-KR(t), the optical Faraday rotation of linearly polarized probe beam upon interaction with the spin-polarized carriers excited by the LCP/RCP pump beam was detected with a Wollaston prism and a balancing Si detector [see Fig. 1(c)].

B. Picosecond time-resolved Kerr effect

Figure 2 reveals the transient quantum beats responses in MAPbBr$_3$ crystal measured by the c-PPR(t) (or t-KR) on two crystal facets, namely [110] and [001] at various fields **B** [see Figs. 1(a) and 1(b)]. For the QB response from the [110] crystal facet, **B** was in the [001] direction, whereas QB from the [001] crystal facet, **B** was aligned along [010]. In our measurements we changed the field strength *B* in the range from 0 to 700 mT. As seen in Fig. 2 the c-PPR(t) measurements reveal two different QB oscillations with frequencies f_1 and f_2 that increase with *B*. The fast QB oscillation corresponds to the electrons, whereas the slow QB oscillation is due to the holes [16–18]. The transient QB response can be fit by two damped harmonic oscillators given by

$$A_1 e^{-t/\tau_1}\cos(2\pi f_1 t + \emptyset 1) + A_2 e^{-t/\tau_2}\cos(2\pi f_2 t + \emptyset 2). \quad (1)$$

In Eq. (1) the time constants τ_1 and τ_2 are the spin dephasing times associated with the electrons and holes, respectively. The fast Fourier transform (FFT) spectra in Fig. 2 inset more clearly reveal the two distinct QB oscillation frequencies, f_1 and f_2. As seen, f_1 and f_2 increase with the field in agreement with the Larmor precession frequency of the electron (hole) spin:

$$\omega = \frac{g\mu_B}{\hbar}B, \quad (2)$$

where $\omega = 2\pi f$. From a linear fit using Eq. (2) [see Figs. 2(d) and 2(h)] we extract the *g*-factor value for electrons, g_e and holes, g_h at each crystal facet, revealing the *g*-value anisotropy in MAPbBr$_3$ crystal. These measurements only determine the magnitude of the *g* factor, but not its polarity. From the fittings we obtained $g_e = 2.15$ (0.03) and 1.75 (0.03) and $|g_h| = 0.42$ (0.02) and 0.60 (0.02) for the [110] and [001] crystal facets, respectively, which represent a wide variation in the *g*-factor tensor.

In addition, we also fit the transient QB response using Eq. (1) and the obtained QB frequencies from Eq. (2) for each field **B** along [001] direction to extract the field-dependent spin-relaxation times for the electrons, τ_e and holes τ_h, as seen in Fig. 3. Remarkably, τ_e ($\sim$1 ns) is much shorter than τ_h ($\sim$8 ns) even at small *B*. Also, τ_e increases at low fields, whereas τ_h does not change much with *B*. We note that both τ_e and τ_h decrease substantially with the excitation intensity, in agreement with recent calculation [19].

We have also measured transient QB response of the electrons and holes in MAPbBr$_3$ *films* at 4 K as seen in Fig. S1(a) [20]. Using the same analysis as for the MAPbBr$_3$ crystal we obtain the electron and hole *g* value as $g_e = 1.83$ for the
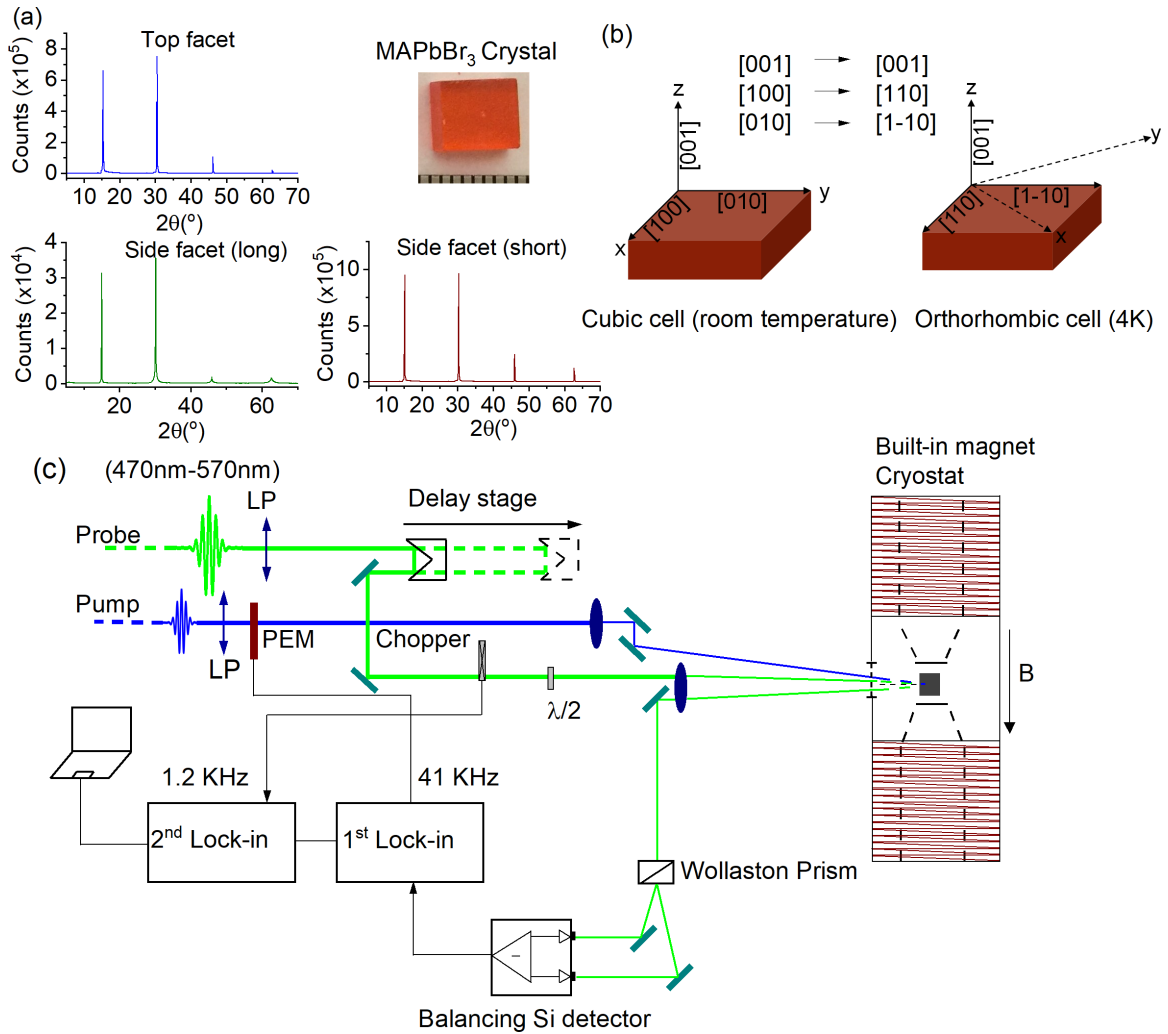
FIG. 1. (a) MAPbBr$_3$ single crystal and its x-ray-diffraction spectra measured on three different facets at room temperature. (b) Crystal-phase transition from cubic cell at room temperature to orthorhombic cell at 4 K. (c) Sketch of the experimental apparatus for nondegenerate pump-probe ps transient Kerr rotation measurement using two lock-in amplifiers. The PEM is a photoelastic modulator for modulating the pump beam circular polarization between left (δ^+) and right (δ^-); $\lambda/2$ is a "half-wavelength plate;" LP is a linear polarizer; and BS is a beam splitter. The MAPbBr$_3$ crystal was mounted in a cryostat and cooled down to 4 K. An electromagnet generates a magnetic field B up to 700 mT in the direction parallel to the crystal surface (i.e., Voigt geometry).

electrons, and $|g_h| = 0.55$ for the holes. It is curious to note that the g values in the unoriented MAPbBr$_3$ film are closer to those of single crystal with **B** along [010]. The reason for this is that the HOIP films with large grains are preferentially aligned with (001) parallel to the surface; that is, the c axis is out of plane (see the Supplemental Material [20]). Therefore, in the Voight configuration with **B** parallel to the film surface, the film g values are dominated by the values in [010]. As a result of the QB response and subsequent determination of the electron and hole g factors, we expect that the exciton g value, $g_{ex} = g_e + g_h$ in MAPbBr$_3$ film measured in the Voight geometry would be $g_{ex} = 2.38$ if g_h is positive, or $g_{ex} = 1.28$ if g_h is negative.

C. Magnetic field-induced circular polarization

It is not possible to determine g_h polarity from the transient QB measurements. In order to determine the g-value polarity

we used the technique of magnetic circular dichroism (MCD) of the excitons in MAPbBr$_3$ thin films at 4 K at B up to 17.5 T in the High Field National Laboratory in Tallahassee, Florida. The MCD technique is described in detail in the Appendix. In this technique, the different absorbance spectra, A, of left ($\sigma+$) and right ($\sigma+$) circular polarized light under high magnetic field is recorded in the Faraday geometry. The MCD spectrum is then obtained from the relation

$$\text{MCD} = A(\sigma+) - A(\sigma-) = -\frac{2\,[T(\sigma+) - T(\sigma-)]}{\ln(10)[T(\sigma+) + T(\sigma-)]},$$
(3)

where $A(\sigma+)[T(\sigma+)]$ and $A(\sigma-)[T(\sigma-)]$ are the respective absorbance [transmission] values of left and right circular polarized light of the film. In the presence of an external magnetic field applied parallel to the light-propagation direction, the two closely exciton states, X and Y in the orthorhombic MAPbBr$_3$ phase, further split, and this leads to an energy
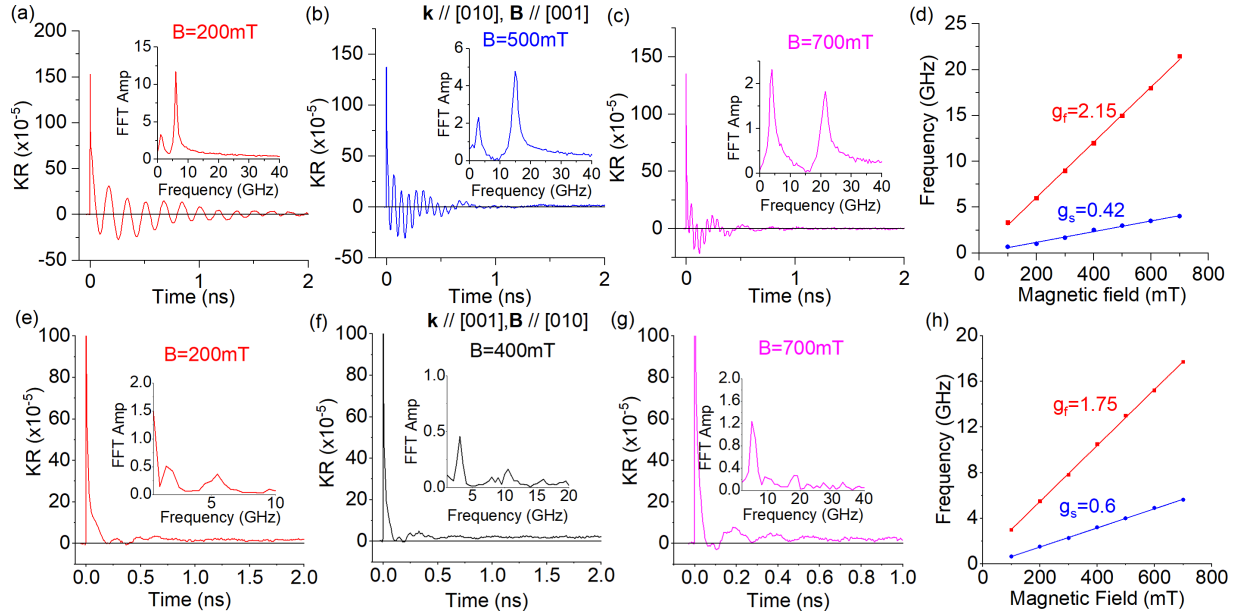
FIG. 2. Photoinduced quantum beatings in MAPbBr$_3$ single crystal excited at 405 nm measured at pump fluence of 1.5 W/cm^2 and at various magnetic field strengths at 4 K. Magnetic field dependence of the transient Kerr rotation dynamics measured on (010) facet with B directed along [001] (a)–(d); and on (001) facet with B along [010] (e)–(h), using probe beam at 552 nm. The insets show the corresponding FFT spectra with two FFT peaks for the fast and slow oscillatory frequencies, respectively. (d), (h) The fast and slow QB frequencies vs B and the anisotropy of the obtained g factors.

difference, ΔE, in the absorption of LCP and RCP light, which, in turn results in a derivative-like MCD spectrum. The relation between the MCD value and the underlying ΔE can be expressed as

$$\mathrm{MCD} = -\frac{dA(E)]}{dE}\Delta E, \qquad (4)$$

In Eq. (4), the Zeeman energy splitting $\Delta E = \mu_B gB$, where μ_B is the Bohr magneton. Figure 4(a) shows the MCD spectra at 4 K for different applied magnetic fields that exhibit a derivative-like feature at the MAPbBr$_3$ exciton absorption band. The MCD magnitude is plotted as a function of field strength in Fig. 4(b), which shows a linear B dependence in agreement with a linear ΔE with B. We fit the MCD(B) dependence using Eq. (4) as seen in Fig. 4(b), from which we obtain the bright exciton g value, $g_{exc} = 2.5 \pm 0.1$ that is related to g_e and g_h via the relation $g_{ex} = g_e + g_h$. From

the QB transient in MAPbBr$_3$ film we measured $|g_e| = 1.83$ and $|g_h| = 0.55$ for **B** in the Voigt geometry. Consequently, in order to satisfy the relation $g_{ex} = g_e + g_h$, we conclude that g_h in MAPbBr$_3$ is positive, similar to g_h in CsPbBr$_3$ [16].

D. Magnetoelectroluminescence response

We have used an additional experimental method to study the g values in MAPbBr$_3$, especially the polarity of the g_h value, namely the magnetoelectroluminescence response, MEL(B) in light-emitting diodes based on MAPbBr$_3$ active layer. For these measurements we fabricated LEDs composed of several layers that include a patterned indium-tin-oxide (ITO)-coated glass; a 30-nm-thick hole transport layer, poly(3,4-ethylenedioxythiophene)
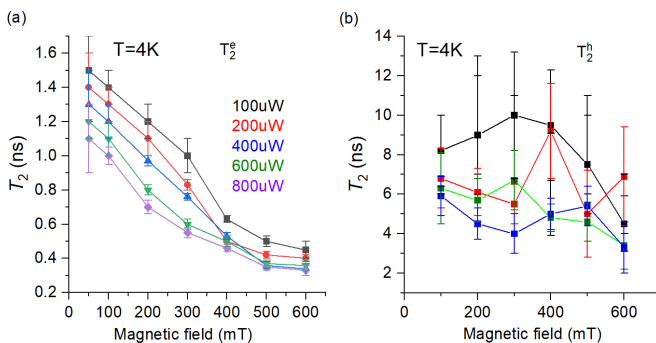

FIG. 3. Magnetic field and excitation power dependencies of the spin lifetime extracted from the fit of the QB dynamics (Fig. 2) using Eq. (1) for electrons (a) and holes (b) at $T = 4$ K.
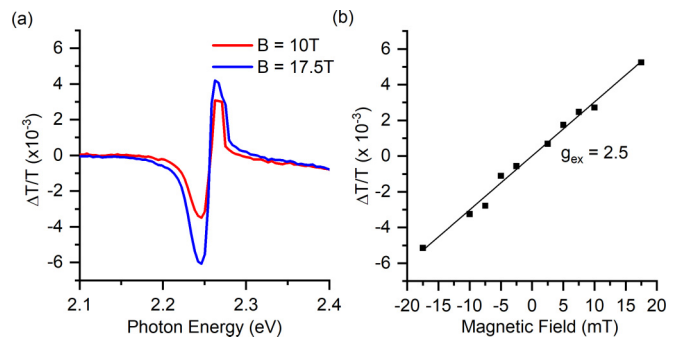

FIG. 4. The MCD spectra of MAPbBr$_3$ at 10 K. (a) The MCD spectra obtained at two magnetic field strengths in the Faraday configuration. (b) The MCD amplitude dependence on the magnetic field and its linear fit. The MCD magnitude is proportional to the Zeeman energy splitting and the g factor is obtained using Eqs. (3) and (4).
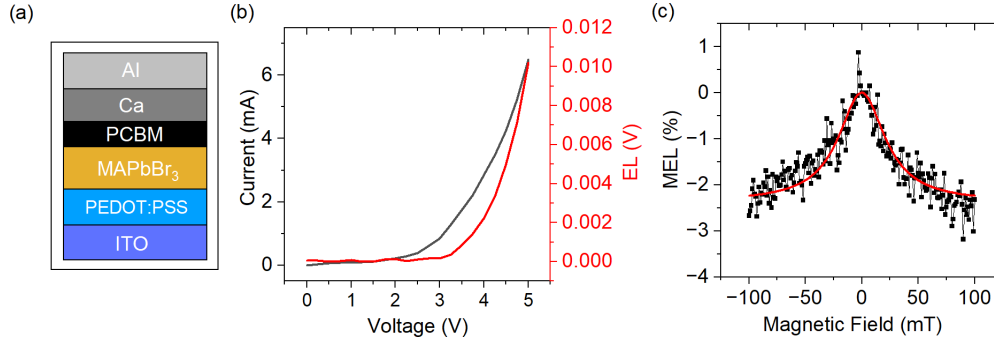
FIG. 5. Magnetoelectroluminescence response measured in a MAPbBr$_3$-based LED device at 10 K. (a) The LED device structure. (b) The *I-V* and EL-*V* characteristic responses of the LED device. (c) The MEL(*B*) response of the integrated EL spectrum measured at 4-V forward bias.

polystyrene sulphonate (PEDOT:PSS); the perovskite active layer; an electron transport layer (phenyl-C61-butyric acid methyl ester); a buffer layer (Ca); and capped with an Al electrode [see Fig. 5(a), inset]. The device was transferred into a vacuum chamber that was placed in an in-plane magnetic field *B* up to 200 mT. The electroluminescence (EL) and MEL measurements were performed at constant bias, V_b, larger than the threshold bias for the EL emission [see EL(*V*) response in Fig. 5(a)]. The MEL(*B*) response is the relative change in the EL intensity upon the application of the field, which is defined as MEL(*B*) = [EL(*B*)–EL(0)]/EL(0), or [EL(*B*)/EL(0) − 1] measured at a constant bias voltage.

The MEL(*B*) response in LEDs is based on *spin mixing* among the four spin sublevels of the injected electron and hole (e-h) pairs, namely e-h singlet (e-h)$_S$ and three e-h triplet (e-h)$_T$ states. The spin-mixing process may be provided by several spin-related interactions such as spin-orbit coupling [21], hyperfine interaction [22,23] and also by the different Landé *g* values of the electron and hole constituents of the e-h pair species, commonly known as the "Δg mechanism" [24]. In the Δg mechanism, the e and h spins in the e-h pair precess around the magnetic field direction, with precession frequency that is linearly dependent on the magnetic field strength and the Landé *g* values of the e and h. If $g_e \neq g_h$, and hence $\Delta g = g_e − g_h \neq 0$, then the e-h pair spin configuration interpolates back and forth between the (e−h)$_S$ and (e−h)$_T$ states many times before steady state is reached. It has been shown that when reaching the steady state, the Δg-mechanism leads to a Lorentzian MEL(*B*) response [25], namely,

$$\mathrm{MEL}(B) = \mathrm{MEL}_{\max}\left[\frac{1}{1 + \left(\frac{B}{B0}\right)^2} - 1\right], \quad B_0 \sim 1/(\mu_B \Delta g\tau),$$
(5)

where MEL(0) = 0, MEL$_{\max}$ is the maximum MEL amplitude at large *B*, and B_0 is the half-width at half maximum of the MEL(*B*) response. For the Δg mechanism it was shown that $B_0 \sim 1/(\mu_B \Delta g\tau)$, where μ_B is the Bohr magneton and τ is the electron or hole spin-relaxation time, whichever is shorter [25].

The MEL(*B*) response of the MAPbBr$_3$-based LED measured at 10 K is shown in Fig. 5(b). As seen, the EL intensity decreases with the field up to 1% in the interval <200 mT. We could fit the MEL(*B*) response using a Lorentzian function

[Eq. (5)] with $B_0 = 25$ mT. This shows that $\Delta g = g_e − g_h \neq 0$ in MAPbBr$_3$. Moreover, we can estimate the spin lifetime, τ_e and τ_e, of the e-h pair species based on the spin-relaxation times extracted from the QB measurements (see Fig. 4). As seen, $\tau_e \ll \tau_h$ and therefore we use τ_e in Eq. (5). It is seen that τ_e increases at low photocarrier density. We estimate that the steady-state electrically injected carrier density in the LED device under operation conditions is about 10^{11} cm^{-3}, which is four orders of magnitude smaller compared with the photocarrier density in the QB measurement ($\sim 10^{15}$ cm^{-3} in the time interval up to 100 ps), so we take $\tau_e = 1.8$ ns to calculate the *maximum* $\Delta g_{\max}$ value from Eq. (5). Consequently we estimate $\Delta g_{\max} = 1.7$ from the MEL response. Since we measured $g_e = 1.83$ in MAPbBr$_3$ film, g_h cannot be negative; otherwise Δg would have been larger than the measured g_e.

E. The *g*-factor calculation

The anisotropic *g* factors have been quantitatively calculated by applying the 8-band **k**·**p** model developed for orthorhombic HOIPs within a quasicubic model [17]. In this model, the Kane energy and Luttinger's magnetic parameter are taken as isotropic, while the anisotropy of the electron and hole *g* factors in the orthorhombic setting derives from the effect of tetragonal and orthorhombic crystal-field parameters δ and ζ, which reflect symmetry breaking relative to the cubic phase in the *z* and in the *x, y* directions, respectively [17,26]. From the best fit to the measured *g* factors (see Supplemental Material, Fig. S2, Ref. [20]) we determine the tetragonal and orthorhombic crystal-field parameters $\delta = -581.1$ meV and $\zeta = 146.3$ meV, respectively; Luttinger's magnetic parameter, $\kappa = +0.052$; and the spin-orbit split-off parameter, $\Delta = 1.116$ eV. In the fits the band gap was constrained to $E_g = 2.246$ eV based on the probe wavelength of 552 nm, which was set in resonance with the exciton, and the Kane energy was constrained to $E_p = 15$ eV based on the value determined from the exciton longitudinal-transverse splitting measured in CsPbBr$_3$ [27]; the initial starting value of the spin-orbit split-off parameter in the fitting procedure was set to $\Delta = 1.5$ eV calculated for CsPbBr$_3$ using hybrid density-functional theory [26]. With the determined best-fit parameters, the calculated electron and hole g factors exactly match the experimental values (the four parameters Δ, δ, ζ, and κ are determined by the four measured *g* factors). The fact that the hole *g* factors are

positive, as determined by the MCD measurement discussed above, is expected within the model given the similarity in band gap to CsPbBr$_3$ which also has a positive hole factor [16,18]. The result stands in contrast to the negative hole g factor found for MAPbI$_3$ [17]. This can be understood most simply given the band-gap energy dependence of the electron and hole g factor in the cubic phase, which can be expressed analytically in the form [17,18]

$$g_e^{\text{cubic}} = \frac{2}{3} \frac{E_p}{E_g} - (4\kappa + 2);$$

$$g_h^{\text{cubic}} = g_0 - \frac{2}{3} E_p \left(\frac{1}{E_g} - \frac{1}{E_g + \Delta} \right), \qquad (6)$$

where $g_0 = |g_e|$ is the free-electron spin g factor ≈ 2. Since the compounds MAPbI$_3$, MAPbBr$_3$, and CsPbBr$_3$ have similar values of the Kane energy and the split-off parameter, the electron g factors are positive while the hole g factors change sign as the band gap is increased from that of MAPbI$_3$ to that of CsPbBr$_3$ as reported in Ref. [18]. In the Supplemental Material, Fig. S3, we plot the band-gap dependence of the electron and hole g factors for the cubic and orthorhombic phases. The figure shows that while the anisotropic g factors for a given carrier type along the [1,0,0], [0,1,0], and [0,0,1] crystallographic directions in the orthorhombic phase individually deviate from the g factors of cubic phase, the average of the orthorhombic g factors for a given carrier type over crystallographic direction shows dependence on the band gap that is the same as that exhibited by the g factors in the cubic phase given by Eq. (6).

F. The dynamic nuclear-spin polarization

In order to reveal the dynamic nuclear-spin polarization (DNSP) associated with our dynamic measurements, the t-KR measurements were performed at low magnetic field, $B < 30$ mT. At such low field, the slow (hole) oscillations were too long to be time resolved; thus, only one oscillation is present in the transient response up to 5 ns. For the standard t-KR setup, the pump is modulated between LCP and RCP and the probe is linearly polarized. This gave us typical results, such as a QB oscillation frequency, f_1, of 811 MHz for the electron precession at an applied field of 30 mT. Importantly, in the standard t-KR there were no oscillations at zero field, as expected; see Fig. 6(a). Upon switching to the c-PPR measurements the pump was still modulated between RCP and LCP, but the probe beam was at a fixed circular polarization. Under these conditions the c-PPR reveals a slow zero-field oscillation that is identified by the signal crossing zero in Fig. 6(b). Figure 6(b) also shows that the LCP/RCP probe causes a shift in f_1. Compared to the linearly polarized probe, the circularly polarized probe increases f_1 to 825 MHz for either LCP or RCP probe, but with a phase change between the two. This is attributed to the geometry of the pump and probe beams in our setup. The probe being perpendicular to the applied magnetic field polarizes the electrons and nuclei spin perpendicular to the magnetic field. Since the nuclei were polarized perpendicularly, the Overhauser field B_N was also perpendicular to the external field. Changing the polarization
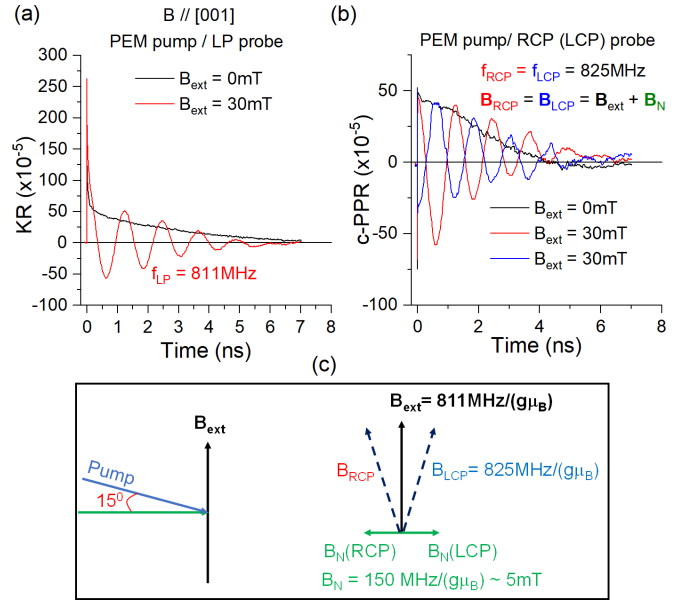

FIG. 6. Dynamic nuclear-spin polarization in MAPbBr$_3$ crystal controlled by the circularly polarized probe beam. (a) Transient Kerr rotation (t-KR) response measured at $B = 0$ (black) and $B = 30$ mT (red) using a circularly polarized pump that is modulated at 41 kHz between LCP and RCP and a linearly polarized probe beam. No zero-field QB oscillation is observed. (b) Transient circularly polarized photoinduced reflection (c-PPR) dynamics measured at $B = 0$ and 30 mT, respectively generated using a modulated LCP/RCP circular polarized pump beam and LCP (red) and RCP (blue) probe-beam polarizations, respectively. The c-PPR at $B = 0$ dynamics (black) show a half-period QB oscillation of ~ 7 ns (i.e., $f_1 < 80$ MHz). (c) The estimated Overhauser field $B_N = 5$ mT that is induced by the circularly polarized probe beam through dynamic nuclear-spin polarization. In the vector diagram, $\mathbf{B}_{RCP/LCP} = \mathbf{B}_N + \mathbf{B}$ is the total field that acts on the carrier spin dynamics.

of the probe beam in our measurement flipped the photocarriers' polarization as seen in Fig. 6(c).

Moreover, we also changed the pump modulation scheme from the helicity modulation (using the PEM) to intensity modulation while keeping constant its circular polarization, either LCP or RCP. Comparing the responses between the standard pump polarization modulation t-KR and the fixed polarization t-KR, there is a clear difference at the zero-field response. With the PEM-modulated helicity, we observed simple decay due to spin relaxation; but, with fixed LCP pump we observed zero-field oscillations similar to the c-PPR measurements at $B > 0$ [Fig. 7(a)], revealing the formation of an internal magnetic field. In addition, as seen at small applied field there was an observed difference in f_1 compared to that in standard t-KR. As demonstrated in Fig. 7(b) with fixed circularly polarized pump beam one helicity increased the QB frequency, whereas the other decreased it. In particular, LCP pump at $B = 30$ mT resulted in $f_1 = 800$ MHz, whereas RCP pump generates $f_1 = 832$ MHz, whereas at the same field of 30 mT the PEM-modulated pump yields QBs of $f_1 = 811$ MHz. The same trend occurs at higher applied field; at $B = 50$ mT, RCP pump gave $f_1 = 1.45$ GHz, whereas LCP pump resulted in $f_1 = 1.40$ GHz compared to $f_1 = 1.42$ GHz that resulted with pump-modulated polarized t-KR
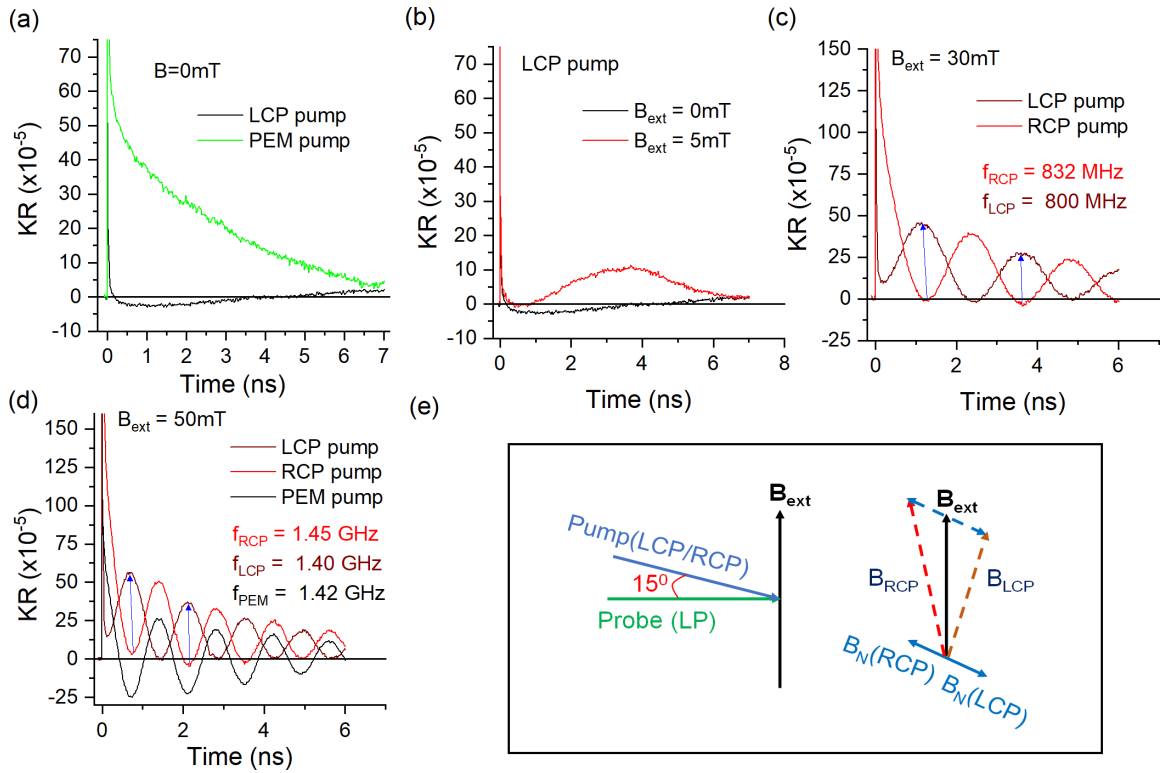
FIG. 7. Dynamic nuclear-spin polarization in MAPbBr$_3$ crystal governed by the circularly polarized pump beam. (a) t-KR response measured at $B = 0$ with LCP pump beam (black) compared with that of pump polarization (green) that is modulated between LCP and RCP at 41 kHz using a photoelastic modulator (PEM). (b) t-KR dynamics measured with a LCP pump beam at $B = 0$ and $B = 5$ mT. (c) t-KR dynamics at $B = 30$ mT excited by LCP (brown) and RCP (red) pump beams, respectively. (d) t-KR dynamics at $B = 50$ mT excited, respectively, by LCP (brown) and RCP (red) pump beams and a circularly modulated pump beam (black). (e) The extracted Overhauser field $B_N = 1.4$ mT induced by the circularly polarized pump beam through dynamic nuclear-spin polarization. In the vector diagram, $\mathbf{B}_{RCP/LCP} = \mathbf{B}_N + \mathbf{B}$ is the overall field that acts on the photocarriers' spin dynamics in the sample.

measurement. Note that compared to the c-PPR results, the pump beam was not perpendicular to the external field. Therefore, B_N is not perpendicular to the external field and a component of B_N adds or subtracts from the external field depending on its polarization, as demonstrated in Fig. 7(c). This explains the reason why one pump helicity increases f_1 while the other helicity decreases it.

III. CONCLUSION

In conclusion, we measured the g factor of electrons and holes and their spin-relaxation dynamics in MAPbBr$_3$ crystal using quantum beats with field direction along two crystal facets which reveal the g-factor tensor anisotropy. We also measured the electron and hole g factors in films that are in agreement with the average g factors in the crystal. Using two additional magneto-optical techniques, namely, MCD in MAPbBr$_3$ films and MEL(B) response in MAPbBr$_3$-based LEDs we determined that the g factor of the hole in this 3D HOIP is positive, similar to the compounds FAPbBr$_3$ and CsPbBr3 [16,18] which have similar band gap.

Additionally, we showed that a variant of the standard t-KR measurement revealed the DNSP and the Overhauser field in a MAPbBr$_3$ crystal. These effects can be observed at a low magnetic field as a shift in the electron QB oscillation frequency. Due to their long lifetimes at He temperature, the DNSP effects are not observed in the standard t-KR measurements since the PEM modulation that switches the pump helicity prevents a net nuclear-spin polarization from occurring in the sample. Using simple geometry, the strength of the Overhauser field can be measured. These measurements revealed an important phenomenon that takes place in the HOIPs and information about the dynamics of the spin of nuclei, which needs to be carefully considered for spintronics applications.

APPENDIX: METHODS

1. Sample preparation

a. MAPbBr3 films. Thin MAPbBr$_3$ films were prepared using a standard procedure with a precursor solution, with CH$_3$NH$_3$Br and PbBr$_2$ in a molar ratio of 1:1 in N,N-dimethylformamide to form a concentration of 0.8 mol/ml. The precursor solution was stirred on the hotplate at 50 °C overnight. The solution was cooled to room temperature and spin coated on glass substrates at 3000 rpm for 60 s. The resulting film was then annealed at 100 °C for 2 h.

b. MAPbBr$_3$ *crystals.* The MAPbBr$_3$ crystals were grown via antisolvent precipitation. A 1 M precursor solution was made by mixing 1.1 g of PbBr$_2$ (Sigma-Aldrich) and 0.34 g of MABr (Sigma-Aldrich) with 3 mL of dimethylformamide. The solution was placed in a vial with no lid, which was in turn placed in a beaker filled with 30 mL of isopropyl alcohol (IPA) capped with punctured Parafilm. The IPA diffused slowly through the precursor solution, initiating crystal growth. After 2 days, MAPbBr$_3$ crystals were retrieved from the solution and dried with N2 compressed gas. XRD measurements confirm the crystal structure and principal axes [see Fig. 1(a)]. Our pump-probe measurements were conducted on a CsPbBr$_3$ crystal at 4 K for two crystal facets, namely (001) and (110) [Fig. 1(a)] with applied magnetic fields parallel to the crystal surface along [010] and [001], respectively [Fig. 1(b)].

2. The time-resolved circular-PPA technique

The picosecond time-resolved circularly polarized photoinduced absorption experiment, c-PPR(t) in MAPbBr$_3$ crystal or PPA(t) in MAPbBr$_3$ film, was utilized to measure the carrier spin dynamics. The pump beam was modulated by a PEM between left (δ^+, or LCP) and right (δ^-, or RCP) circular polarization. The probe beam, which was tuned in resonance with the exciton absorption peak at 552 nm, was also circularly polarized (LCP in our case) using a quarter-wave plate. We measured the transient change in the probe-beam transmission (or reflection) induced by LCP and RCP pump polarizations, $\Delta T_{\delta^- \delta^+}^{\delta^+ \delta^+} = T_{\delta^+ \delta^+} - T_{\delta^- \delta^+}$ (or $\Delta R_{\delta^- \delta^+}^{\delta^+ \delta^+} = R_{\delta^+ \delta^+} - R_{\delta^- \delta^+}$ for circular PPR). For the pump- and probe beams we used a variety of nonlinear optical crystals. The 405-nm pump pulse was generated by doubling the frequency of the fundamental Ti:sapphire beam at 776 nm using second-harmonic generation in a BBO crystal. The probe beam at 552 nm was generated by phase matching the 776-nm beam from the Ti-sapphire laser and a 1919-nm beam from the optical parametric oscillator laser onto a nonlinear sum-frequency BBO crystal. The pump-probe setup time resolution was 250 fs at 80-MHz repetition rate. Both pump- and probe beams were aligned through various optical components to spatially and temporally overlap onto the small area of the samples loaded in the closed-loop helium cryostat (Montana Instrument). The pump and probe beam sizes were ∼130 μm for the pump and 100 μm for the probe. The probe pulse was mechanically delayed with respect to the pump pulse by a translation stage. For detection we used a silicon photodetector connected to two lock-in amplifiers (LIA) in series. One LIA was externally synchronized with the chopper frequency at 1.2 kHz for mea-

suring the probe transmission, whereas the second LIA was externally synchronized with the PEM frequency at 41 kHz.

3. The MCD measurements

The MCD and optical absorption spectroscopies were carried out in the 25-T Split-Florida Helix magnet at the National High Magnetic Field Laboratory with optical fiber accessible custom sample holder. The incident-light wavelength from a 300-W tungsten lamp was varied by an Oriel monochromator with bandwidth ∼1 nm. The excitation light was subsequently modulated into left- and right circularly polarized light using a PEM from Hinds Instruments, whereas an optical chopper operating at 377 Hz measured the background transmission through the film. The excitation light was focused by a pair of lenses onto the sample, whereas a monochromator was used to scan the wavelength in steps of 1 nm. The transmitted light was collected by an optical fiber and directed onto a Si photodetector. The signal was preamplified before being electrically connected to a Stanford SR 830 lock-in amplifier. The difference and sum of left and right circularly transmitted light were recorded in the Faraday geometry by two lock-in amplifiers having a common input from the photodetector, and operating at different reference signals from the PEM and a chopper, respectively. The sample temperature was kept at 10 K.

The absorbance of the excitonic transition was approximated by a Gaussian line shape: $A(E) = A_0 \exp[-(E - E_0)^2 / 2w^2]$, where A_0 is the amplitude, $2w$ is the linewidth, and E_0 is the photon energy of the exciton band. Under a perpendicular magnetic field, we work under the assumption that the circularly polarized MAPbBr$_3$ exciton states split, resulting in two oppositely circularly polarized transitions at energies $E_0 \pm \frac{1}{2}\Delta E$, where $\Delta E = g\mu_B B$ is the Zeeman energy. The difference of left/right circular polarized light absorbance peaks with energies $E_0 \pm \frac{1}{2}\Delta E$ is given by $\Delta A = A(E_0 + \frac{1}{2}\Delta E) - A(E_0 - \frac{1}{2}\Delta E) = \frac{dA}{dE}\Delta E$. The relation between the experimentally obtained MCD $\Delta T/T$ signal and ΔA is expressed as $\Delta A = \log(\frac{\Delta T}{T} + 1)$ that may be Taylor expanded into $(\Delta T/T)$ since it is relatively small $\Delta A \approx 1/\ln(10) \Delta T/T$. A_0 and w for each exciton band were obtained from fitting the respective optical absorbance spectrum.

4. The LED device engineering

The LEDs were, respectively, composed of a patterned ITO-coated glass; an ≈ 30-nm-thick hole transport layer (PEDOT:PSS); the perovskite active layer; an electron transport layer (PCBM); a buffer layer (Ca); and capped with an Al electrode.

The CH$_3$NH$_3$PbBr$_3$ hybrid perovskite precursor solution was made from mixing 0.5 M of CH$_3$NH$_3$Br (Dyenamo) with 0.5 M of PbBr$_2$ (Sigma-Aldrich) in anhydrous N,N-dimethylformamide (Alfa Aesar). We used ITO-coated glass as substrates, which were precleaned sequentially with deionized water, acetone, and isopropanol for 15 min by means of ultrasonic bath, respectively. Subsequently the substrates were dried by nitrogen blow and treated with oxygen plasma for 8 min. The perovskites LED devices were fabricated on patterned ITO-coated glass (15–20 ohms per

square, Luminescence Tech.). We deposited an $\sim$30-nm-thick hole transport layer, poly(3,4-ethylenedioxythiophene) polystyrene sulphonate (PEDOT:PSS, Clevios P VP AI 4083), that was annealed in air for 20 min at $140\,^\circ$C. The perovskite solution was spin coated at 3000 rpm and annealed on a hot plate at $100\,^\circ$C for 30 min. Once cooled, a 25-mg ml^{-1} solution of phenyl-C70-butyric acid methyl ester (PC$_{71}$BM) dissolved in anhydrous chlorobenzene (Sigma-Aldrich) was spin coated at 1000 rpm. The device was capped with a Ca (20 nm)/Al (100 nm) electrode that was thermally evaporated through a shadow mask defining an active area of ≈ 4 mm^2.

5. The MEL measurements

For the MEL measurements, the perovskite LED devices were transferred into a vacuum chamber that was placed in an in-plane magnetic field B up to 200 mT. The transport and MEL measurements were performed in a cryostat at 10 K. The I-V characteristic response was obtained using a standard four-point method with a Keithley 236 power supply and Keithley 2000 multimeter. The EL and MEL measurements were performed at constant bias, V_b. To avoid interference with the wire magnetoconductance we used electrical wires made of metallic alloys to keep the parasitic magnetoresistance below 0.001%. The EL emission was monitored with a silicon detector. The LED devices were operated at forward bias $V_b > V_{th}$, where V_{th} is the threshold bias voltage for the EL, while sweeping the external magnetic field in one direction and back for several cycles to improve the signal-to-noise ratio. The MEL is defined as MEL$(B) = [\text{EL}(B)/\text{EL}(0) - 1]$ measured at a constant bias voltage.

[1] Y. C. Kim, Y. Porte, S-D. Baek, S. R. Cho, and J-M. Myoung, High-performance green light-emitting diodes based on MAPbBr$_3$–polymer composite films prepared by gas-assisted crystallization, ACS Appl. Mater. Interfaces **9**, 44106 (2017).

[2] Y. Liang, Y. Wang, C. Mu, S. Wang, X. Wang, D. Xu, and L. Sun, Achieving high open-circuit voltages up to 1.57 V in hole-transport-material-free MAPbBr$_3$ solar cells with carbon electrodes, Adv. Energy Mater. **8**, 1701159 (2018).

[3] H. Mehdi, A. Mhamdi, R. Hannachi, and A. Bouazizi, MAPbBr$_3$ perovskite solar cells via a two-step deposition process, RSC Adv. **9**, 12906 (2019).

[4] N. Giesbrecht, J. Schlipf, L. Oesinghaus, A. Binek, T. Bein, P. Müller-Buschbaum, and P. Docampo, Synthesis of perfectly oriented and micrometer-sized MAPbBr$_3$ perovskite crystals for thin-film photovoltaic applications, ACS Energy Lett. **1**, 150 (2016).

[5] J. Yao, Q. Pan, Z.-J. Feng, Y.-A. Xiong, T.-T. Sha, H.-R. Ji, Z.-X. Gu, and Y.-M. You, Hybrid organic–inorganic perovskite ferroelectrics bring light to semiconducting applications: Bandgap engineering as a starting point, APL Mater. **9**, 040901 (2021).

[6] M-J. Wu, C-C. Kuo, L-S. Jhuang, P-H. Chen, Y-F. Lai, and F-C. Chen, Bandgap engineering enhances the performance of mixed-cation perovskite materials for indoor photovoltaic applications, Adv. Energy Mater. **9**, 1901863 (2019).

[7] L. Protesescu, S. Yakunin, M. Bodnarchuk, F. Krieg, R. Caputo, C. H. Hendon, R. X. Yang, A. Walsh, and M. V. Kovalenko, Nanocrystals of cesium lead halide perovskites (CsPbX$_3$, X = Cl, Br, and I): Novel optoelectronic materials showing bright emission with wide color gamut, Nano Lett. **15**, 3692 (2015).

[8] J. H. Noh, S. H. Im, J. H. Heo, T. N. Mandal, and S. I. Seok, Chemical management for colorful, efficient, and stable inorganic–organic hybrid nanostructured solar cells, Nano Lett. **13**, 1764 (2013).

[9] B. Wenger, P. K. Nayak, X. Wen, S. V. Kesava, N. K. Noel, and H. J. Snaith, Consolidation of the optoelectronic properties of CH3NH3PbBr3 perovskite single crystals, Nat. Commun. **8**, 590 (2017).

[10] R. Wang, S. Hu, X. Yang, X. Yan, H. Lia, and C.-X. Sheng, Circularly polarized photoluminescence and Hanle effect measurements of spin relaxation in organic–inorganic hybrid perovskite films, J. Mater. Chem. C **6**, 2989 (2018).

[11] S. Yang, E. Vetter, T. Wang, A. Amassian, and D. Sun, Observation of long spin lifetime in MAPbBr$_3$ single crystals at room temperature, J. Phys. Mater. **3**, 015012 (2020).

[12] R. P. Sabatini, C. Liao, S. Bernardi, W. Mao, M. S. Rahme, A. Widmer-Cooper, U. Bach, S. Huang, A. W. Y. Ho-Baillie, and G. Lakhwani, Solution-processed Faraday rotators using single crystal lead halide perovskite, Adv. Sci. **7**, 1902950 (2020).

[13] M. Zhou, J. S. Sarmiento, C. Fei, X. Zhang, and H. Wang, Effect of composition on the spin relaxation of lead halide perovskites, Phys. Chem. Lett. **11**, 1502 (2020).

[14] A. Kostadinov-Mutzafi, J. Tilchin, A. Shapiro, D. N. Dirin, M. V. Kovalenko, L. Z. Tan, and E. Lifshitz, Impact of anisotropy in spin-orbit coupling on the magneto-optical properties of bulk lead halide perovskites, Phys. Rev. B **106**, 035303 (2022).

[15] E. Kirstein, D. R. Yakovlev, M. M. Glazov, E. Evers, E. A. Zhukov, V. V. Belykh, N. E. Kopteva, D. Kudlacik, O. Nazarenko, D. N. Dirin, M. V. Kovalenko, and M. Bayer, Lead-dominated hyperfine interaction impacting the carrier spin dynamics in halide perovskites, Adv. Mater. **34**, 2105263 (2022).

[16] U. N. Huynh, T. Feng, D. R. Khanal, H. Liu, P. Bailey, R. Bodin, P. C. Sercel, J. Huang, and Z. V. Vardeny, Transient and steady state magneto-optical studies of the CsPbBr3 crystal, Phys. Rev. B **106**, 094306 (2022).

[17] U. N. Huynh, Y. Liu, A. Chanana, D. R. Khanal, P. C. Sercel, J. Huang, and Z. V. Vardeny, Transient quantum beatings of trions in hybrid organic tri-iodine perovskite single crystal, Nat. Commun **13**, 1428 (2022).

[18] E. Kirstein, D. R. Yakovlev, M. M. Glazov, E. A. Zhukov, D. Kudlacik, I. V. Kalitukha, V. F. Sapega, G. S. Dimitriev, M. A. Semina, M. O. Nestoklon, E. L. Ivchenko, N. E. Kopteva, D. N. Dirin, O. Nazarenko, M. V. Kovalenko, A. Baumann, J. Höcker, V. Dyakonov, and M. Bayer, The Landé factors of electrons and holes in lead halide perovskites: Universal dependence on the band gap, Nat. Commun. **13**, 3062 (2022).

[19] J. Xu, K. Li, U. N. Huynh, J. Huang, R. Sundararaman, Z. V. Vardeny, and Y. Ping, How spin relaxes and dephases in bulk halide perovskites, Nat. Commun. **15**, 188 (2024).

[20] See Supplemental Material at http://link.aps.org/supplemental/10.1103/PhysRevB.109.014316 for the calculation of g factors in orthorhombic MAPbBr$_3$; supplemental data figures for Figs. S1–S4; and supplemental tables S1 and S2 for the g-value calculation. The Supplemental Material also includes Refs. [28–32].

[21] J. Rybicki, T. D. Nguyen, Y. Sheng, and M. Wohlgenannt, Spin-orbit coupling and spin relaxation rate in singly charged π-conjugated polymer chains, Synth. Met. **160**, 280 (2010).

[22] T. D. Nguyen, B. R. Gautam, E. Ehrenfreund, and Z. V. Vardeny, Magnetoconductance response in unipolar and bipolar organic diodes at ultrasmall fields, Phys. Rev. Lett. **105**, 166804 (2010).

[23] T. D. Nguyen, G. Hukic-Markosian, F. Wang, L. Wojcik, X. G. Li, E. Ehrenfreund, and Z. V. Vardeny, Isotope effect in spin response of π-conjugated polymer films and devices, Nat. Mater. **9**, 345 (2010).

[24] C. Zhang, D. Sun, C. X. Sheng, Y. X. Zhai, K. Mielczarek, A. Zakhidov, and Z. V. Vardeny, Magnetic field effects in hybrid perovskite devices, Nat. Phys. **11**, 427 (2015).

[25] A. H. Devir-Wolfman, B. Khachatryan, B. R. Gautam, L. Tzabary, A. Keren, N. Tessler, and E. Ehrenfreund, Short-lived charge-transfer excitons in organic photovoltaic cells studied by high-field magneto-photocurrent, Nat. Commun **5**, 4529 (2014).

[26] P. C. Sercel, J. L. Lyons, N. Bernstein, and Al. L. Efros, Quasicubic model for metal halide perovskite nanocrystals, J. Chem. Phys. **151**, 234106 (2019).

[27] D. R. Yakovlev, S. A. Crooker, M. A. Semina, J. Rautert, J. Mund, D. N. Dirin, M. V. Kovalenko, and M. Bayer, Exciton-polaritons in CsPbBr$_3$ crystals revealed by optical reflectivity in high magnetic fields and two-photon spectroscopy, arXiv:2307.07035.

[28] J. Even, L. Pedesseau, J.-M. Jancu, and C. Katan, Importance of spin–orbit coupling in hybrid organic/inorganic perovskites for photovoltaic applications, J. Phys. Chem. Lett. **4**, 2999 (2013).

[29] Z. G. Yu, Effective-mass model and magneto-optical properties in hybrid perovskites, Sci. Rep. **6**, 28576 (2016).

[30] J. Even, L. Pedesseau, C. Katan, M. Kepenikian, J.-S. Lauret, D. Sapori, and E. Deleporte, Solid-state physics perspective on hybrid perovskite semiconductors, J. Phys. Chem. C **119**, 10161 (2015).

[31] J. M. Luttinger, Quantum theory of cyclotron resonance in semiconductors: General theory, Phys. Rev. **102**, 1030 (1956).

[32] P.-O. Löwdin, A note on the quantum-mechanical perturbation theory, J. Chem. Phys. **19**, 1396 (1951).